PAPER

Check for updates

Structure prediction of mixed-anion perovskites: systematic approach integrating octahedral tilting and anion ordering†

Sanni Määttänen and Antti J. Karttunen [iD] *

We present a systematic workflow for the structure prediction of mixed-anion perovskites. We consider both octahedral tilting and anion ordering in perovskites to predict potential new oxyfluoride, oxynitride, and nitrofluoride perovskites. The workflow is as follows: (1) pre-screen potential mixed-anion perovskite compositions with the τ tolerance factor, (2) build anion-ordered structure models for 11 perovskite tilt systems, (3) filter the ordered models with a machine-learning methodology, and (4) compare the energetics of the predicted mixed-anion perovskites to experimentally known reference compounds using hybrid density functional methods. We studied 16 novel mixed-anion perovskite compositions, where each composition included approximately 200 000 anion-ordered models. Of these 16 studied mixed-anion perovskite compositions, six are predicted to be energetically favorable compared to experimentally known competing phases.

1 Introduction

Perovskites form a versatile class of functional materials where both the cation and anion composition can be tuned systematically.[1] Ferroelectric perovskite oxides are used extensively for example in piezoelectric and pyroelectric applications,[2,3] and further improvement of their dielectric properties is of great interest. Synthesis of mixed-anion perovskites is one of the key strategies to adjust the material properties in a controlled way. For example, the dielectric properties of prototypical ferroelectric perovskite oxide $BaTiO_3$ can be improved by synthesizing an oxynitride derivative of it.[4]

The general formula of the perovskite structure type is ABX_3, where A is usually a larger cation located in the corner of the unit cell, B is a medium-sized cation located in the center of the unit cell and X is an anion located in the faces of the unit cell (Fig. 1a). The B cation is octahedrally coordinated with six anions and in the ideal cubic perovskite structure, the octahedron is not tilted with respect to the lattice vectors.[1] Although oxygen is the most common and extensively studied anion in perovskites, other non-metals, such as nitrogen[5-7]

and fluorine can be included as anions.[8,9] Heavier halogen congeners Cl, Br, and I can also serve as anions.[10]

Combinations of different anions in the perovskite structure type lead to mixed-anion perovskites (ABX_2Y). Compared to oxide perovskites, mixed-anion perovskites are less studied, even though they have interesting properties and possibilities due to the different anionic characteristics.[11] In many mixed-anion perovskites the anion sites are crystallographically fully disordered, but there are also many examples of anion-ordered mixed-anion perovskites.[5,6] Understanding the energetics of anion-ordered crystal structures is also the starting point for developing more advanced models for mixed-anion perovskites with anion disorder. In this work, the focus is on anion-ordered ABO_2N, ABO_2F, ABF_2O, ABF_2N, and ABN_2F mixed-anion perovskites.

1.1 Oxynitride, oxyfluoride, and nitrofluoride perovskites

Unlike oxide perovskites, several oxynitride perovskites are brightly colored.[12] For example, $LaTaO_2N$ and $CaTaO_2N$ are potential non-toxic color pigments.[13] In addition to their use as pigments, oxynitrides could have applications as photocatalysts[12] thanks to their optoelectronic properties.[14] The band gap could also be tuned by varying the N/O ratio.[6] For example, $LaTiO_2N$ has shown photoreactions under visible light.[15] Furthermore, oxynitrides could be used as capacitors because of their high dielectric constant.[16] Especially tantalum oxynitrides exhibit high dielectric constants.[6]

Similarly to oxynitride perovskites, oxyfluoride perovskites can also exhibit interesting properties related for example to

Department of Chemistry and Materials Science, Aalto University, P.O. Box 16100, FI-00076 Aalto, Finland. E-mail: antti.karttunen@aalto.fi

†Electronic supplementary information (ESI) available: Input files used to generate the used ordered models, additional crystallographic details for the used models, benchmarks for the used computational methods, information on experimental reference compounds, and bond length analyses. See DOI: https://doi.org/10.1039/d5dt01139f
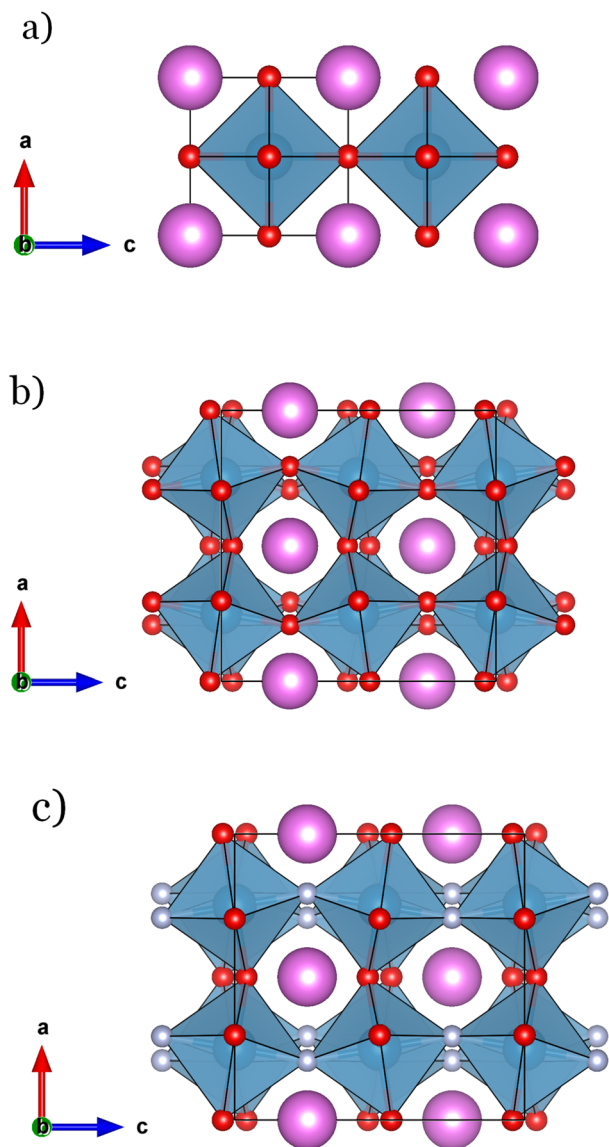
Fig. 1 Three perovskite-type structures viewed along *b* axis: (a) ideal ABX$_3$ structure (*Pm3̄m*), (b) ABX$_3$ structure with tilted octahedra ($a^+b^0c^-$ tilt system, *Cmcm*), (c) mixed-anion perovskite ABX$_2$Y structure with tilted octahedra ($a^+b^0c^-$ tilt system). A-cations drawn in pink, B-cations and their octahedra in blue, X-anions in red, and Y-anions in grey.

ferroelectricity and multiferroicity.[9] Several oxyfluoride perovskites exhibit exciting magnetic properties.[17,18] Insertion of F anions in the structure introduces more defects, which might enable ionic conductivity.[19]

Compared to oxynitrides and oxyfluorides, nitrofluoride perovskites (or fluoride nitrides) have received limited attention in research.[9] According to the Inorganic Crystal Structure Database (ICSD),[20] not a single nitrofluoride perovskite is known experimentally. Only LaMgF$_2$N[21,22] and LaZrN$_2$F[23] have been studied computationally to our knowledge. Nitrofluorides represent an intriguing new class of compounds that may exhibit properties similar to oxynitride and oxyfluoride perovskites.

As the number of mixed-anion perovskites is still limited compared to oxide perovskites, there is plenty of room for the exploration of new mixed-anion perovskite chemistries. Quantum chemical methods and AI-driven structure prediction approaches offer powerful strategies to predict and discover new mixed-anion perovskite compositions. However, in order to obtain robust predictions of thermodynamically stable perovskites for experimental work, it is crucial to use realistic structure models where octahedral tilting is considered explicitly.

1.2 Octahedral tilting of perovskites

Both in the case of single-anion and mixed-anion perovskites, the octahedra around the B cation can tilt in order to achieve a lower energy structure.[1,24,25] Fig. 1b illustrates an ABX$_3$ perovskite structure with tilted octahedra. The tilting of rigid BX$_6$ octahedra is the most common distortion mechanism in perovskites, allowing the A–X distances can be shortened while the first coordination sphere of the B cation remains unchanged.[24]

The standard approach for describing octahedral tilting is the Glazer notation,[26] in which tilting along the *x*-, *y*- and *z*-axes is represented by the letters *a*, *b*, and *c*. Superscripts 0, +, and − indicate whether tilting occurs along *a*, *b*, or *c* direction. Octahedra in two adjacent layers can tilt in the same direction (+) or in opposite direction (−) along the tilt axis.

According to Glazer, there are a total of 23 distinct tilt systems.[26] However, a detailed group theoretical analysis shows that eight of the original Glazer tilt systems have too high symmetry relative to the space group, which explains why they are not observed in real structures.[27] Additionally, Lufaso and Woodward reported in 2001 that four of the remaining 15 tilt systems are transitional or low-symmetry tilt systems.[28] Here we limit the analysis of tilt systems to the 11 remaining tilt systems.[28]

In the majority of computational structure prediction studies on perovskite-type materials, octahedral tilting has not been systematically considered. Shojaei and Yin studied octahedral tilting of 18 different halide perovskites with Density Functional Theory (DFT) methods.[29] They concluded that for every studied perovskite, the untilted structure was energetically the least stable. Xie *et al.* studied octahedral tilting of CsSnI$_3$ perovskite and also concluded that the untilted structure was energetically the least stable.[30] Bechtel and van der Ven studied four halide perovskites and showed the untilted structure to be the least stable tilt system for all the studied perovskites.[31] Albrecht and Karttunen investigated the role of octahedral tilting in the case of ferroelectric CaMnTi$_2$O$_6$ double perovskite.[32] Overall, the previous studies highlight the importance of systematically including octahedral tilting in computational high-throughput studies on potential new perovskites.

Here we use quantum chemical methods and consider both octahedral tilting and anion ordering to predict potential new oxyfluoride, oxynitride, and nitrofluoride perovskites. We present a systematic workflow where we (1) pre-screen poten-

tial mixed-anion perovskite compositions with the τ tolerance factor,[33] (2) build anion-ordered structure models for all 11 tilt systems, (3) filter the ordered models with a machine-learning (ML) methodology, and (4) compare the energetics of the predicted mixed-anion perovskites to experimentally known reference compounds using hybrid DFT methods.

2 Methods

The workflow used in this study included several steps that are discussed in the following subsections. First, the selection of the studied perovskite compositions is presented in subsection 2.1. Treatment of tilt systems and anion ordering is discussed in subsection 2.2, and the ML-based filtering methodology for ordered models is presented in subsection 2.3. Computational details for DFT calculations are given in subsection 2.4, and the energy ranking of ordered models is explained in 2.5. Finally, the energy comparisons between the predicted mixed-anion perovskites and experimentally known competing phases are discussed in subsection 2.6.

2.1 Selection of perovskite compositions using tolerance factor τ

We focused on the following mixed-anion perovskites with O, N, and F anions: ABO_2N, ABO_2F, ABF_2O, ABF_2N, and ABN_2F. In the case of B cation, we limited the study to non-magnetic and non-toxic d-metal cations Sc(III), Y(III), La(III), Ti(IV), Zr(IV), Nb (V), Ta(V), and Mo(VI). For the A cation, we considered all non-radioactive elements whose common oxidation state would lead in a neutral compound in combination with the B cation and anions. For example, for ABO_2N perovskite with B = Mo(VI) and anion oxidation states adding up to −VII, the oxidation state of the A cation needs to be +I. The number of potential perovskite compositions remaining after the element selection is shown in the column II of Table 1.

After the initial filtering of compounds based on elemental composition, their potential to form a stable perovskite structure was estimated using ionic radii. The Goldschmidt tolerance factor t can be used to estimate whether the cations and anions are likely to form a perovskite.[34] However, in 2019, Bartel *et al.* showed that the tolerance factor t predicts correctly only 74% of potential perovskite compounds.[33] In their study, Bartel *et al.* proposed a new, more accurate, tolerance factor

$$\tau = \frac{r_x}{r_B} - n_A \left(n_A - \frac{r_A/r_B}{\ln(r_A/r_B)} \right) \tag{1}$$

where r_A and r_B are the ionic radii of the A and B cations, r_x is the ionic radius of the anion and n_A is the oxidation state of the A cation. When $\tau < 4.18$, the structure is predicted to form a perovskite structure in ambient pressure.[33] Nevertheless, neither tolerance factor takes into account the octahedral tilting, which can strongly affect the energetics of the perovskite structure.

We carried out pre-screening of possible perovskite structures with tolerance factor τ using Shannon ionic radii.[35] For the mixed-anion perovskites, the ionic radius of the anion was calculated as the average of the ionic radii of the two anions. The compounds with $\tau < 5$ were selected for further analysis. The number of compounds with $\tau < 5$ is shown in the column III of Table 1. Out of these compounds, we selected for detailed analysis 16 compounds that are composed of relatively common elements and do not contain highly toxic elements (column IV of Table 1).

2.2 Tilt systems and anion ordering

The tilt systems and anion ordering were studied systematically for the selected compounds presented in column IV of Table 1. The initial tilt system models were derived from a previous study that provided crystal structures of $CaMnTi_2O_6$ double perovskite in 11 tilt systems.[32] The Mn atom was first replaced with Ca, resulting in 11 tilt system models of composition $CaTiO_3$ and Z varying from 1 to 8. The tilt systems with their Glazer notation and space group are listed in columns 1–3 of Table 2.

Table 1 The number of potential mixed-anion perovskite compositions during the selection process

(I) Perovskite	(II) Cation selection	(III) $\tau < 5$	(IV) Selected compounds
ABO_2N	151	47	$AgMoO_2N$ $KMoO_2N$ $NaMoO_2N$ $YTiO_2N$
ABO_2F	72	24	$KZrO_2F$ $NaTiO_2F$ $SrScO_2F$
ABF_2O	24	14	$KScF_2O$ KYF_2O $NaScF_2O$
ABN_2F	151	42	$BaNbN_2F$ $LaTiN_2F$ $LaZrN_2F$
ABF_2N	72	24	$BaScF_2N$ $KTiF_2N$ $KZrF_2N$

Table 2 Glazer notation, space group, number of anion site distributions, and number of ordered structures for each tilt system. The number of ordered structures for each tilt system is a sum of ordered structures from different anion site distributions. Tilt system 11 is the untilted structure

Tilt	Glazer notation	Space group	Distributions	Structures
1	$a^+a^+a^+$	204 $Im\bar{3}$	1	16 000
2	$a^+a^+c^-$	137 $P4_2/nmc$	45	50 000
3	$a^-b^+a^-$	62 $Pnma$	5	23 000
4	$a^-b^-b^-$	15 $C2/c$	5	23 000
5	$a^-a^-a^-$	167 $R\bar{3}c$	1	500
6	$a^0b^+b^+$	139 $I4/mmm$	9	24 000
7	$a^+b^0c^-$	63 $Cmcm$	45	50 000
8	$a^0b^-b^-$	74 $Imma$	5	14 000
9	$a^0a^0c^+$	127 $P4/mbm$	3	4000
10	$a^0a^0c^-$	140 $I4/mcm$	5	6000
11	$a^0a^0a^0$	221 $Pm\bar{3}m$	1	3000

The anion-ordered models for mixed-anion perovskites were created with the SUPERCELL code.[36] The number of anion sites and their multiplicity determines how many anion-ordered models each tilt system has. The number of anion sites varies from 1 to 3 in different tilt systems and the anion ratio is always X_2Y. For example, tilt system 1 has one anion site (Wyckoff position $24g$), meaning that the site has 16 X anions and 8 Y anions. For comparison, tilt system 2 has three atom sites (Wyckoff positions $8g$, $8g$, and $8f$) and there are 45 different ways to distribute the anions on these sites. A detailed listing of the Wyckoff positions and anion distributions for all tilt systems is given in ESI (Table S1†). The number of anion distributions for each tilt system is listed in column 4 of Table 2.

For tilt systems with $Z < 8$, the anion-ordered models were generated for a supercell with $Z = 8$ (except for trigonal tilt system 5 where $Z = 6$). We used the *merge* option of SUPERCELL to identify identical ordered models and keep only one of them. SUPERCELL input files used to generate the ordered models are included as ESI.† Each anion distribution results in a different number of ordered structures, varying from 1 to over 14 000 (see Table S1†). Within the 11 tilt systems, the total number of ordered structures varies from 500 to 50 000 (column 5 in Table 2), and the total number of anion-ordered structures for the 11 tilt systems is approximately 200 000.

2.3 ML-based filtering of ordered models

DFT structure optimizations and energy comparisons for the 200 000 anion-ordered structures for each of the 16 studied compounds would require excessive computational resources. Therefore, we implemented a pre-screening of the ordered models with computationally less intensive methods. The SUPERCELL code includes a built-in feature that calculates the Coulomb energy of the ordered models based on the formal charges of the elements. We first carried out a benchmark study for the experimentally known $SrTaO_2N$ perovskite. We compared the relative energies from the SUPERCELL Coulomb approach with DFT-calculated energies. The comparison revealed that DFT calculations and SUPERCELL Coulomb calculations provided very different energy ranking for anion-ordered models (Fig. S1 in ESI†).

As the energy rankings provided by SUPERCELL Coulomb energies and DFT relative energies were not in good agreement, we benchmarked the M3Gnet universal graph deep learning interatomic potential.[37] Compared to SUPERCELL Coulomb energies, M3Gnet energy rankings for $SrTaO_2N$ were in better agreement with DFT energy rankings (Fig. S2†). However, the M3Gnet relative energies are not in full agreement with DFT relative energies and it is recommended to use M3Gnet only to filter out high-energy ordered models before DFT calculations. While we applied M3Gnet in the workflow presented here, it is possible to use any other machine-learning potential such as the most accurate potentials from the Matbench Discovery leaderboard.[38]

Finally, we compared the energy rankings from SUPERCELL Coulomb energies and M3Gnet for 5000 anion-ordered models of experimentally known $BaTaO_2N$ perovskite (Fig. S3†). The comparison demonstrated that the lowest-energy M3Gnet ordered models were among approximately 700 lowest-energy structures based on SUPERCELL. Therefore, in our final workflow, we first generated the 1000 lowest-energy ordered models for each anion distribution with SUPERCELL. Then, we calculated the relative energies of these ordered models with M3Gnet. From each anion distribution, the five lowest-energy ordered models predicted by M3Gnet were then used for further energy comparisons. For anion distributions with less than five ordered structures, all ordered structures were included in the further energy comparisons.

2.4 Computational details for DFT calculations

The CRYSTAL23[39] program was utilized for quantum chemical calculations. The DFT-PBE0 hybrid density functional method[40,41] was used in combination with all-electron, Gaussian-type basis sets derived from the Karlsruhe def2 basis sets.[42,43] Polarized triple-zeta-valence Karlsruhe-type basis sets (TZVP) were employed for the d-metals, O, N, and F. Split-valence + polarization basis sets (SVP) were employed for group 1 and 2 elements. The reason for using a somewhat smaller SVP-level basis set for group 1 and 2 elements is that elements such as Na, K, Sr, or Ba in ionic solids do not typically participate extensively in covalent bonding. The calculations were carried out with the Coulomb and exchange integral tolerance factors (TOLINTEG) set to tight values of 8, 8, 8, 8, and 16. Monkhorst–Pack -type k-meshes for the reciprocal space sampling[44] were chosen in such way that k-point density was similar for all studied systems (as an example, a $4 \times 4 \times 4$ mesh would be used for a primitive cubic system with $a = 5$ Å). Atomic positions and lattice parameters were fully optimized within constraints imposed by the space group symmetry. Harmonic vibrational frequencies were calculated for selected structures to confirm them as true local minima.[45] Partial charges of B cations and anions were analyzed with Mulliken population analysis. Detailed results of bond length and partial charge analyses are presented as ESI (Table S4†).

2.5 Energy ranking of ordered models

After the M3Gnet energy ranking of the ordered models within each tilt system, 1–10 lowest-energy ordered models from each tilt system were studied with the DFT-PBE0 method. The number of ordered models used from each tilt system was based on the relative M3Gnet energies. Full DFT structural optimizations were then carried out on the lowest-energy ordered models of each tilt system to provide a final ranking of the lowest-energy ordered models. For each ordered model, we calculated its relative energy ΔE with respect to the lowest-energy ordered model (reported in kJ per mol per formula unit). Finally, harmonic frequency calculations were carried out for the lowest-energy ordered models to confirm that they represent true local minima.

2.6 Energy comparison with experimentally known compounds

After the full analysis of tilt systems and anion orderings, we have the lowest-energy ordered model of each compound. In the final step of the workflow, we investigate the experimental feasibility of the compound by comparing the lowest-energy ordered model with experimentally known competing phases. As an example, the reaction energy for the formation of SrScO$_2$F from SrO and ScOF would be as follows:

$$SrO(s) + ScOF(s) \rightarrow SrScO_2F(s) \qquad (2)$$

The reaction energy ΔE_r the reaction can then be calculated as:

$$\Delta E_r = E(SrScO_2F) - E(SrO) - E(ScOF), \qquad (3)$$

where E (compound) is the total energy of the compound. If $\Delta E_r < 0$, the mixed-anion perovskite is energetically more favorable than the experimental reference compounds. The experimental reference compounds and the reactions used for calculating ΔE_r for all studied perovskites are given in ESI (Table S2†). The crystal structures of the comparison compounds were obtained from Inorganic Crystal Structure Database (ICSD) and they were fully optimized in similar way to the studied perovskites. The oxidation states of the metal ions are similar in the experimental reference compounds and the predicted perovskites, except for Nb(III)N which is then oxidized to BaNb(V)N$_2$F. In the case of ScN (competing phase for BaScF$_2$N), single point energy calculated for the experimental crystal structure was used in the calculation of ΔE_r due to technical issues. ΔE_r for BaScF$_2$N is over 200 kJ mol^{-1} and it is thus unlikely that it could be synthetized.

3 Results

The structure prediction workflow could be fully completed for 14 compounds of the 16 studied mixed-anion perovskites (two of the hypothetical perovskites, AgMoO$_2$N and LaTiN$_2$F, appear unlikely since the DFT calculations failed). For one of the studied hypothetical compounds, KTiF$_2$N, the predicted lowest-energy structure is not a proper perovskite structure. Six of the hypothetical mixed-anion perovskites are energetically more favorable than experimentally known reference structures. The studied compounds, their τ values, lowest-energy tilt systems, and other information are presented in Table 3. The band gaps of the ABO$_2$F and ABF$_2$O oxyfluoride perovskites are larger than the band gaps of the perovskites containing nitrogen anions. A more detailed analysis of the studied perovskites is presented below in subsections 3.1–3.5.

The untilted ideal perovskite structure (tilt system 11) was the lowest-energy structure for only two of the studied perovskites. For the other mixed-anion perovskites, the lowest-energy ordered model was a tilted structure, which highlights the importance of including octahedral tilting in perovskite structure prediction workflows. The relative energies of the tilt

Table 3 A summary of τ values and the lowest-energy anion-ordered models of the compounds studied in this work. The tilt system and space group of the lowest-energy structure are presented for each compound, together with the band gap and reaction energy ΔE_r. If $\Delta E_r < 0$, the mixed-anion perovskite is energetically more favorable than the experimental reference compounds. All structures in the table are true local minima, except for BaScF$_2$N

Compound	τ	Lowest-energy tilt system	Space group of the lowest-energy ordered model	Band gap (eV)	ΔE_r (kJ mol^{-1})
AgMoO$_2$N	3.94	Not converged			
KMoO$_2$N	3.59	11, $a^0a^0a^0$	Cc	3.6	−139
NaMoO$_2$N	3.77	9, $a^0a^0c^-$	$P1m1$	1.5	−109
YTiO$_2$N^a	4.46	3, $a^-b^+a^-$	$P2_1/c$	3.4	−117
KZrO$_2$F	3.58	11, $a^0a^0a^0$	$Pmma$	5.9	35
NaTiO$_2$F	3.53	5, $a^-a^-a^-$	$P3_221$	4.9	10
SrScO$_2$F	4.17	10, $a^0a^0c^-$	$C2/c$	7.1	−62
KScF$_2$O	3.53	5, $a^-a^-a^-$	$C2/c$	6.8	18
KYF$_2$O	3.87	5, $a^-a^-a^-$	$P1$	6.5	72
NaScF$_2$O	3.97	8, $a^0b^-b^-$	$I2_12_12_1$	6.8	43
BaNbN$_2$F	3.51	5, $a^-a^-a^-$	$P\bar{1}$	1.3	−8
LaTiN$_2$F	1.97	Not converged			
LaZrN$_2$F	3.40	4, $a^-b^-b^-$	$P2_1/c$	3.9	−62
BaScF$_2$N^b	3.59	1, $a^+a^+a^+$	$Pmmn$	3.5	221
KTiF$_2$N^c	3.64	5, $a^-a^-a^-$	$P1$	3.9	0
KZrF$_2$N	3.56	5, $a^-a^-a^-$	$P3_221$	4.9	83

^{a} In the case of YTiO$_2$N, SVP-quality basis set for used for screening of the tilt systems. The energy comparisons to existing compounds were carried out with higher-level TZVP basis set. ^{b} Not a true local minimum, shows imaginary frequencies. ^{c} The lowest-energy structure does not exhibit a perovskite structure due to a long distance between the B cation and the anions. The second lowest-energy structure, however, has a perovskite structure with an energy difference of 6.4 kJ mol^{-1} to the lowest-energy structure.

systems vary significantly for the studied perovskites (Fig. 2). In Fig. 2, only the lowest-energy ordered model of each tilt system is presented. Table S3 in the ESI† includes additional relative energies for the ordered models within each tilt system.

3.1 ABO$_2$N compounds

Of the four studied ABO$_2$N compounds, AgMoO$_2$N showed severe convergence problems in DFT calculations and was left out of the final comparisons. In the case of KMoO$_2$N, NaMoO$_2$N, and YTiO$_2$N, a few of the tilt systems converged successfully and exhibited a perovskite structure. For NaMoO$_2$N, only ordered models of tilt systems 9 and 11 were perovskites. The other tilt systems showed no band gap in the calculations and were therefore excluded from further studies. The optimized structures of KMoO$_2$N, NaMoO$_2$N, and YTiO$_2$N perovskites are predicted to be energetically favorable in comparison to experimentally known reference compounds.

The relative energies of tilt systems for ABO$_2$N perovskites are presented in Fig. 2a. For KMoO$_2$N, the untilted tilt system 11 is clearly the lowest-energy tilt system. Relative energy difference between the lowest-energy and the second lowest-energy tilt system is over 100 kJ mol^{-1} for KMoO$_2$N. For NaMoO$_2$N and YTiO$_2$N, tilt systems 9 and 3 are the lowest-
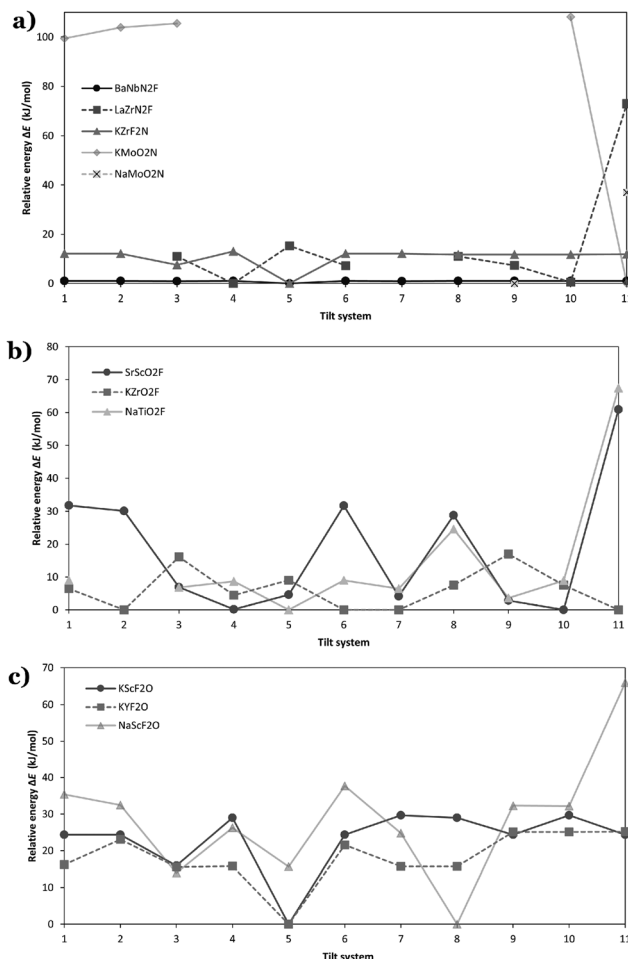
Fig. 2 Relative energies (ΔE) of the tilt systems in the studied mixed-anion perovskites: (a) ABN_2F, ABF_2N, and ABN_2O perovskites (b) ABO_2F perovskites, and (c) ABF_2O perovskites. The lowest-energy anion-ordered model for each tilt system is shown in the plot. For the lowest-energy tilt system, $\Delta E = 0$. The relative energies are given per formula unit. The figure does not include tilt systems where DFT calculations failed.

energy tilts, respectively. $YTiO_2N$ is not shown in **2** because a smaller SVP-level basis set was applied to pre-screen the tilt systems due to numerical issues and the larger TZVP-level basis set was used only to compare the lowest-energy ordered model with experimental reference compounds.

3.2 ABO_2F compounds

The structure prediction workflow was successfully completed for the three studied ABO_2F compounds, and all compounds exhibited a perovskite structure. $SrScO_2F$ is predicted to be energetically favorable over the experimentally known reference compounds. The band gap of $SrScO_2F$ is significantly larger in comparison to $KZrO_2F$ and $NaTiO_2F$ (7.1 eV). The relative energies of the tilt systems for ABO_2F perovskites are presented in Fig. 2b. For both $SrScO_2F$ and $NaTiO_2F$, the untilted, ideal tilt system (tilt system 11) is the highest in energy. In addition, the energy of the untilted tilt system is sig-

nificantly higher compared to the tilt system with the second-highest energy. On the other hand, for $KZrO_2F$ the untilted tilt system is the lowest-energy tilt system. However, for $KZrO_2F$ the tilt systems 2, 6, and 7 are very close in energy to the lowest-energy tilt system 11.

3.3 ABF_2O compounds

The structure prediction workflow was successfully completed for the three studied ABF_2O compounds and the compounds exhibited a perovskite structure. The band gaps of the three ABF_2O perovskites are rather large and close to each other (6.5–6.8 eV). None of the ABF_2O perovskites are energetically favorable in comparison to experimental reference compounds. The relative energies of tilt systems for ABF_2O perovskites are presented in Fig. 2c. For all three perovskites, the untilted tilt system 11 is among the highest-energy structures. For KYF_2O and $NaScF_2O$, tilt system 11 is the highest-energy tilt system. Compared to other studied perovskites, the energy difference between the lowest-energy tilt system and the second lowest-energy tilt system is larger in ABF_2O perovskites.

Both $KScF_2O$ and KYF_2O have potassium as the A cation and the relative energies of the tilt systems are rather similar. For both perovskites, tilt system 5 is the lowest energy tilt system. On the other hand, the relative energies of tilt systems in $NaScF_2O$ and $KScF_2O$ differ clearly, even though they both have scandium as the B cation. This is in line with the fact that the octahedral tilting is typically related to the changes in A–X distances in the structure.[24]

3.4 ABN_2F compounds

The structure prediction workflow for $BaNbN_2F$ and $LaZrN_2F$ was successful and the compounds possess a perovskite structure. $LaTiN_2F$ showed severe convergence problems in DFT calculations and was left out of the final comparisons. Band gaps of $BaNbN_2F$ and $LaZrN_2F$ are smaller compared to band gaps of ABO_2F and ABF_2O. The band gap of $BaNbN_2F$ is only 1.3 eV. Both $BaNbN_2F$ and $LaZrN_2F$ are energetically favorable over the experimental reference compounds.

The relative energies of tilt systems for ABN_2F perovskites are presented in Fig. 2a. For $BaNbN_2F$, the relative energies do not differ significantly from each other. For $LaZrN_2F$, there are few tilt systems with low relative energies but for the most tilt systems, the relative energies differ from each other. The untilted ideal tilt system is clearly the highest-energy tilt system for $LaZrN_2F$.

3.5 ABF_2N compounds

Of the three ABF_2N compounds, the structure prediction workflow succeeded for $KTiF_2N$ and $KZrF_2N$. For $BaScF_2N$, the final harmonic frequency calculations indicated that the structure prediction workflow did not reach a true local minimum. Even though the optimization of $KTiF_2N$ succeeded, the bond length between B cations and anions is very large, and therefore, $KTiF_2N$ does not exhibit a real perovskite structure. Out of the three ABF_2N compounds, only $KZrF_2N$ exhibited a perovskite structure and it is higher in energy in comparison to

experimental reference structures. The relative energies of tilt systems for $KZrF_2N$ are presented in Fig. 2a. The tilt system 5 is the lowest-energy tilt system and the energies of the other tilt systems do not differ significantly from each other.

3.6 Comparison of bond lengths and partial charges

For each perovskite, the bond lengths of B–X and B–Y bonds were compared between the different tilt systems. Detailed bond length and partial charge analyses for all studied compounds are given in the ESI (Table S4†) and only the main findings are discussed here. For all of the perovskites, the B–F bond is longer than the B–O/N bond. Depending on the perovskite, bond lengths vary differently in relation to tilt systems. For $KMoO_2N$, $KScF_2O$, KYF_2O, and $NaNbN_2F$ perovskites, in the lowest-energy tilt system, the shortest and longest B–X and B–Y bonds differ clearly. For the higher-energy tilt systems, both B–X and B–Y bonds become more similar in length. For $KMoO_2N$, only Mo–N bonds become more similar. On the other hand, in the lowest-energy tilt system of $KZrO_2F$, $NaTiO_2F$, $SrScO_2F$, and $NaScF_2O$, the shortest and longest B–X bonds are very close in length to each other. The same is true for the shortest and longest B–Y bonds. For most of these perovskites, the bond lengths of B–X and B–Y become more similar to each other in the higher-energy tilt systems. Thus, in the lowest-energy tilt system, all of the bonds forming the octahedra are similar to each other. $KZrO_2F$ is an exceptional case where the shortest and longest Zr–O and Zr–F bonds become different from each other as the relative energy of the tilt system increases. For most of the studied perovskites, the positive Mulliken partial charge of B cation decreases as the relative energy of the tilt system increases. For each perovskite, the changes in partial charges are relatively small and the trends are not analysed here in detail (see Table S4† for the data).

4   Discussion

The compounds with $\Delta E_r < 0$ in Table 3 are lower in energy compared to experimentally known reference phases. Because no crystal structures have been reported for the predicted perovskite-type phases in the ICSD, these compositions could be interesting synthesis targets. We note that the structure prediction workflow used here does not yet include entropic effects.[5] Consideration of the entropic contributions is needed to determine the thermodynamic stability at finite temperatures, while the results here are based on 0 K electronic energies. Therefore, we cannot predict whether a certain mixed-anion perovskite would possess anion-ordered or disordered crystal structure based on the present results. A large energy difference between the lowest-energy anion-ordered crystal structure and other anion-ordered models could indicate that ordering is possible. If the energy difference between anion-ordered models is small, it is more likely that a disordered mixed-anion perovskite would form. In any case, the results reported here suggest that in computational studies towards novel

mixed-anion perovskite compositions it is useful to consider both the tilt systems and the anion ordering systematically.

As shown in Fig. 2c, the ABF_2O perovskites show a significant energy difference of over almost 20 kJ per mol per formula unit between the lowest-energy and the second lowest-energy tilt systems. Furthermore, in $NaScF_2O$, the lowest-energy ordered model is 9.7 kJ mol^{-1} lower in energy compared to the next ordered model in energy ranking. These findings suggest that $NaScF_2O$ could exhibit an anion-ordered structure based on energetical arguments, but the ΔE_r of $NaScF_2O$ is clearly positive and it is not likely to be thermodynamically stable. For perovskites with negative ΔE_r, only $KMoO_2N$ has a clear energy differences between the tilt systems. However, the energy difference between the lowest-energy ordered model and the next ordered model in energy ranking is only 0.8 kJ mol^{-1}. Robust predictions on the anion ordering would require also consideration of entropic effects.

$SrScO_2F$ is one of the mixed-anion perovskites where ΔE_r is predicted to be clearly negative. A related compound with the same elemental composition but different stoichiometry, Sr_2ScO_3F, is experimentally known.[46] Based on our calculations, the reaction energy for $SrScO_2F + SrO \rightarrow Sr_2ScO_3F$ is -5.5 kJ mol^{-1}, suggesting Sr_2ScO_3F to be lower in energy compared to $SrScO_2F$.

Although the mixed-anion perovskites studied here have not been synthetized, several of them have been previously studied computationally. However, octahedral tilting has not been systematically included in previous studies. Wang *et al.* have conducted an extensive computational study of oxynitride, oxyfluoride and nitrofluoride perovskites with DFT methods.[21] The authors studied approximately 120 ABO_2F and 130 ABF_2O perovskites. Among these compounds were also $KZrO_2F$, $NaTiO_2F$, $SrScO_2F$, $KScO_2F$, KYO_2F and $NaScO_2F$ studied here. They used DFT-PBE as the exchange–correlation functional, while DFT-PBE0 method was used in this work. In their stability analysis Wang *et al.* studied both the ideal cubic perovskite structure as well as structures distorted with Pymatgen.[47] Structure distortions included both tilting and rotation of octahedra, as well as rearrangement of anions. The most significant difference between this work and the study of Wang *et al.*, is ΔE_r of $SrScO_2F$. Based on the results of this work, $SrScO_2F$ was found to be energetically lower than competing experimentally known phases ($\Delta E = -62$ kJ per mol per Z). However, Wang *et al.* reported the formation energy of a distorted $SrScO_2F$ model to be 62 meV per atom (30 kJ per mol per Z). For an ideal perovskite structure, their formation energy was 83 kJ per mol per Z. The difference to our study can be explained by different formalism to calculate the formation energy, systematic consideration of octahedral tilting and the different DFT exchange–correlation functional.

Sawada and Nakajima have studied approximately 3300 oxynitride and oxide perovskites with DFT-PBE, including $KMoO_2N$ and $NaMoO_2N$ studied here.[48] They predicted both $KMoO_2N$ and $NaMoO_2N$ to be stable based on their formation enthalpies. Their formation enthalpies for $KMoO_2N$ and $NaMoO_2N$ were -0.12 eV per atom (-58 kJ per mol per Z) and

−0.060 eV per atom (−29kJ per mol per Z), respectively. The ΔE_r values from our calculations are even lower compared to Sawada and Nakajima (Table 3). In our study, the lowest-energy tilt system of $KMoO_2N$ is the ideal tilt system 11 which Sawada and Nakajima studied, as well. Therefore, the octahedral tilting does not explain the somewhat different energetics for $KMoO_2N$ and most likely the differences can be explained by selection of the reference compounds and different DFT methods. In the case of $NaMoO_2N$, we predict the lowest tilt system to be tilt system 9 and not the ideal tilt system 11.

Young *et al.* studied the thermodynamic stability and anion ordering of perovskite oxynitrides with DFT methods.[49] They did not explicitly consider different tilt systems, but the unit cells were allowed to relax in their structural optimizations to accommodate tilt patterns. The compounds studied in their paper are different from those studied here.

Although nitrofluoride perovskites have been studied only to a limited extent, Matar and Demazeau have used DFT-PBE to examine $LaZrN_2F$.[23] They conducted a stability analysis with the same reference compounds as in this work. Based on their results, a postperovskite structure of $LaZrN_2F$ is a stable compound with ΔE_r of −0.96 eV per Z (−93 kJ/mol per Z). The ΔE_r of Matar and Demazeau is more favorable for $LaZrN_2F$ compared to our value of −62 kJ/mol per Z. In the postperovskite structure, the octahedra are highly tilted which can explain the even lower ΔE_r. The different result can also be explained at least partially with different exchange–correlation functional.

5 Conclusions

We have presented a systematic workflow where we (1) pre-screen potential mixed-anion perovskite compositions with the τ tolerance factor, (2) build anion-ordered structure models for all 11 tilt systems, (3) filter the ordered models with a machine-learning methodology, and (4) compare the energetics of the predicted mixed-anion perovskites to experimentally known reference compounds using hybrid DFT methods. For several mixed-anion perovskites, the untilted ideal tilt system was the highest-energy tilt system with energy difference of tens of kJ per mol per formula unit compared to the lowest-energy tilt system. Our findings highlight the importance of integrating octahedral tilting and anion ordering in the study of mixed-anion perovskites. We predict $KMoO_2N$, $NaMoO_2N$, $YTiO_2N$, $SrScO_2F$, $BaNbN_2F$, and $LaZrN_2F$ to be lower in energy in comparison to experimentally known reference compounds. For these mixed-anion perovskites, the energy differences between the lowest-energy ordered models are relatively small and they might show anion disorder if synthetized. The methodology reported here can be applied to any mixed-anion perovskite with composition ABX_2Y, and the resulting low-energy ordered models can be used in further studies on the key functional properties of the perovskite materials.

Author contributions

Sanni Määttänen: investigation, visualization, writing – original draft preparation, writing – review and editing. Antti. J. Karttunen: conceptualization, writing – review and editing, supervision, and funding acquisition. All authors have read and agreed to the published version of the manuscript.

Conflicts of interest

There are no conflicts to declare.

Data availability

The data supporting this article have been included as part of the ESI.†

Acknowledgements

References

1 R. J. Tilley, *Perovskites: Structure-Property Relationships*, John Wiley & Sons, 2016.

2 C. R. Bowen, H. A. Kim, P. M. Weaver and S. Dunn, *Energy Environ. Sci.*, 2014, **7**, 25–44.

3 C. R. Bowen, J. Taylor, E. LeBoulbar, D. Zabek, A. Chauhan and R. Vaish, *Energy Environ. Sci.*, 2014, **7**, 3836–3856.

4 T. Wang, F. Gong, X. Ma, S. Pan, X.-K. Wei, C. Kuo, S. Yoshida, Y.-C. Ku, S. Wang, Z. Yang, S. Hazra, K. H. L. Zhang, X. Liu, Y. Tang, Y.-L. Zhu, C.-F. Chang, S. Das, X. Ma, L. Chen, B. Xu, V. Gopalan, L. Bellaiche, L. W. Martin and Z. Chen, *Sci. Adv.*, 2025, **11**, eads8830.

5 J. P. Attfield, *Cryst. Growth Des.*, 2013, **13**, 4623–4629.

6 A. Fuertes, *J. Mater. Chem.*, 2012, **22**, 3293.

7 A. Fuertes, *Prog. Solid State Chem.*, 2018, **51**, 63–70.

8 R. Needs and M. Weller, *J. Solid State Chem.*, 1998, **139**, 422–423.

9 H. Hyrondelle, A. Terry, J. Lhoste, S. Tencé, K. Lemoine, J. Olchowka, D. Dambournet, C. Tassel, J. Gamon and A. Demourgues, *Chem. Rev.*, 2025, **125**, 4287–4358.

10 K. Sandeep, K. Padmakumar, K. U. Ambili, P. Jishnu, K. H. Fousia, A. R. Ramesh, J. P. Rappai, V. Santhi and M. Shanthil, *Phys. Status Solidi B*, 2022, **259**, 2100600.

11 H. Kageyama, K. Hayashi, K. Maeda, J. P. Attfield, Z. Hiroi, J. M. Rondinelli and K. R. Poeppelmeier, *Nat. Commun.*, 2018, **9**, 772.

12 S. G. Ebbinghaus, H.-P. Abicht, R. Dronskowski, T. Müller, A. Reller and A. Weidenkaff, *Prog. Solid State Chem.*, 2009, **37**, 173–205.

13 M. Jansen and H.-P. Letschert, *Nature*, 2000, **404**, 980–982.

14 I. E. Castelli, K. S. Thygesen and K. W. Jacobsen, *J. Mater. Chem. A*, 2015, **3**, 12343–12349.

15 A. Kasahara, K. Nukumizu, G. Hitoki, T. Takata, J. N. Kondo, M. Hara, H. Kobayashi and K. Domen, *J. Phys. Chem. A*, 2002, **106**, 6750–6753.

16 Y.-I. Kim, P. M. Woodward, K. Z. Baba-Kishi and C. W. Tai, *Chem. Mater.*, 2004, **16**, 1267–1276.

17 M. Sturza, H. Kabbour, S. Daviero-Minaud, D. Filimonov, K. Pokholok, N. Tiercelin, F. Porcher, L. Aldon and O. Mentré, *J. Am. Chem. Soc.*, 2011, **133**, 10901–10909.

18 O. Clemens, F. J. Berry, A. J. Wright, K. S. Knight, J. Perez-Mato, J. Igartua and P. R. Slater, *J. Solid State Chem.*, 2013, **206**, 158–169.

19 M. Sturza, S. Daviero-Minaud, H. Kabbour, O. Gardoll and O. Mentré, *Chem. Mater.*, 2010, **22**, 6726–6735.

20 D. Zagorac, H. Müller, S. Ruehl, J. Zagorac and S. Rehme, *J. Appl. Crystallogr.*, 2019, **52**, 918–925.

21 H.-C. Wang, J. Schmidt, S. Botti and M. A. L. Marques, *J. Mater. Chem. A*, 2021, **9**, 8501–8513.

22 M. Jain, D. Gill, S. Monga and S. Bhattacharya, *J. Phys. Chem. C*, 2023, **127**, 15620–15629.

23 S. F. Matar and G. Demazeau, *Chem. Phys. Lett.*, 2010, **498**, 77–80.

24 P. M. Woodward, *Acta Crystallogr., Sect. B:Struct. Sci.*, 1997, **53**, 32–43.

25 P. M. Woodward, *Acta Crystallogr., Sect. B:Struct. Sci.*, 1997, **53**, 44–66.

26 A. M. Glazer, *Acta Crystallogr., Sect. B*, 1972, **28**, 3384–3392.

27 C. J. Howard and H. T. Stokes, *Acta Crystallogr., Sect. B: Struct. Sci.*, 1998, **54**, 782–789.

28 M. W. Lufaso and P. M. Woodward, *Acta Crystallogr., Sect. B:Struct. Sci.*, 2001, **57**, 725–738.

29 F. Shojaei and W.-J. Yin, *J. Phys. Chem. C*, 2018, **122**, 15214–15219.

30 N. Xie, J. Zhang, S. Raza, N. Zhang, X. Chen and D. Wang, *J. Phys.:Condens. Matter*, 2020, **32**, 315901.

31 J. S. Bechtel and A. Van der Ven, *Phys. Rev. Mater.*, 2018, **2**, 025401.

32 E. K. Albrecht and A. J. Karttunen, *Dalton Trans.*, 2022, **51**, 16508–16516.

33 C. J. Bartel, C. Sutton, B. R. Goldsmith, R. Ouyang, C. B. Musgrave, L. M. Ghiringhelli and M. Scheffler, *Sci. Adv.*, 2019, **5**, eaav0693.

34 V. M. Goldschmidt, *Naturwissenschaften*, 1926, **14**, 477–485.

35 R. D. Shannon, *Acta Crystallogr., Sect. B*, 1976, **32**, 751–767.

36 K. Okhotnikov, T. Charpentier and S. Cadars, *J. Cheminf.*, 2016, **8**, 1–15.

37 C. Chen and S. P. Ong, *Nat. Comput. Sci.*, 2022, **2**, 718–728.

38 J. Riebesell, R. E. A. Goodall, P. Benner, Y. Chiang, B. Deng, G. Ceder, M. Asta, A. A. Lee, A. Jain and K. A. Persson, *Nat. Mach. Intell.*, 2025, **7**, 836–847.

39 A. Erba, J. K. Desmarais, S. Casassa, B. Civalleri, L. Donà, I. J. Bush, B. Searle, L. Maschio, L. Edith-Daga, A. Cossard, C. Ribaldone, E. Ascrizzi, N. L. Marana, J.-P. Flament and B. Kirtman, *J. Chem. Theory Comput.*, 2023, **19**, 6891–6932.

40 J. P. Perdew, K. Burke and M. Ernzerhof, *Phys. Rev. Lett.*, 1996, **77**, 3865.

41 C. Adamo and V. Barone, *J. Chem. Phys.*, 1999, **110**, 6158–6170.

42 F. Weigend and R. Ahlrichs, *Phys. Chem. Chem. Phys.*, 2005, **7**, 3297–3305.

43 M. S. Kuklin, K. Eklund, J. Linnera, A. Ropponen, N. Tolvanen and A. J. Karttunen, *Molecules*, 2022, **27**, 874.

44 H. J. Monkhorst and J. D. Pack, *Phys. Rev. B*, 1976, **13**, 5188–5192.

45 F. Pascale, C. M. Zicovich-Wilson, F. López Gejo, B. Civalleri, R. Orlando and R. Dovesi, *J. Comput. Chem.*, 2004, **25**, 888–897.

46 Y. Wang, K. Tang, B. Zhu, D. Wang, Q. Hao and Y. Wang, *Mater. Res. Bull.*, 2015, **65**, 42–46.

47 S. P. Ong, W. D. Richards, A. Jain, G. Hautier, M. Kocher, S. Cholia, D. Gunter, V. L. Chevrier, K. A. Persson and G. Ceder, *Comput. Mater. Sci.*, 2013, **68**, 314–319.

48 K. Sawada and T. Nakajima, *APL Mater.*, 2018, **6**, 101103.

49 S. D. Young, J. Chen, W. Sun, B. R. Goldsmith and G. Pilania, *Chem. Mater.*, 2023, **35**, 5975–5987.